ACS APPLIED MATERIALS & INTERFACES

Research Article

www.acsami.org

High Performance All-Solid-State Flexible Micro-Pseudocapacitor Based on Hierarchically Nanostructured Tungsten Trioxide Composite

Xuezhen Huang,[¶] Hewei Liu,[¶] Xi Zhang, and Hongrui Jiang*

Materials Science Program, Department of Electrical and Computer Engineering, University of Wisconsin-Madison, Madison, Wisconsin 53706, United States

Supporting Information

ABSTRACT: Microsupercapacitors (MSCs) are promising energy storage devices to power miniaturized portable electronics and microelectromechanical systems. With the increasing attention on all-solid-state flexible supercapacitors, new strategies for high-performance flexible MSCs are highly desired. Here, we demonstrate all-solid-state, flexible micro-pseudocapacitors via direct laser patterning on crack-free, flexible WO_3/polyvinylidene fluoride (PVDF)/multiwalled carbon nanotubes (MWCNTs) composites containing high levels of porous hierarchically structured WO_3 nanomaterials (up to 50 wt %) and limited binder (PVDF, <25 wt %). The work leads to an areal capacitance of 62.4 mF·cm^{-2} and a volumetric capacitance of 10.4 F·cm^{-3}, exceeding that of graphene based flexible MSCs by a factor of 26 and 3, respectively. As a noncarbon based flexible MSC, hierarchically nanostructured WO_3 in the narrow finger electrode is essential to such enhancement in energy density due to its pseudocapacitive property. The effects of WO_3/PVDF/MWCNTs composite composition and the dimensions of interdigital structure on the performance of the flexible MSCs are investigated.

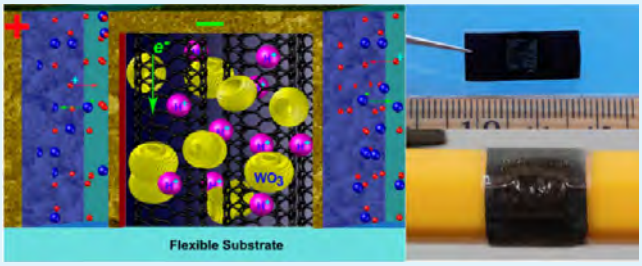

KEYWORDS: *nanomaterials, energy storage, tungsten oxide, microsupercapacitors, laser patterning*

INTRODUCTION

Microsupercapacitors (MSCs) with 3-dimensional (3D) interdigital structures have attracted much attention due to the unique on-chip design for energy storage and its advantage in the enhancement of energy density.[1−6] With the ever increasing use of portable electronic devices, all-solid-state flexible SCs have caught much interest.[3,7−11] Flexible MSCs, which circumvent the limitations of rigid substrates and are potentially compatible with reel-to-reel production, are especially promising. Carbon materials, such as graphene or carbon nanotubes (CNTs), have been utilized in MSCs;[3,7] they are also the only materials showing favorable flexibility so far.[12] Nonetheless, the aggregation and restacking problems of graphene during fabrication processes cause a low capacitance by hampering ionic access to the surfaces. Nanostructured metal oxides with several oxidation states have been widely investigated for energy storage applications owing to the presence of pseudocapacitive.[8,13−15] To date, pseudocapacitive materials based flexible 3D MSCs, particularly with a scalable fabrication method, have not been reported. On one hand, introducing pseudocapacitive nanomaterials into electrodes for capacitors with traditional processes involving solvent evaporation, drying, or annealing often creates mud cracks because of shrinkage-related biaxial tensile stresses, leading to unstable and even poor performance of devices.[16] On the other hand, it remains challenging to form and maintain the micron-sized interdigital structures on flexible materials.

WO_3 has high pseudocapacitance, resulting from electrochemical intercalation/deintercalation with protons following the application of a low voltage, represented as[17,18]

$$WO_3 + xH^+ + xe^- \leftarrow\rightarrow H_xWO_3 \quad (1)$$

Its high intrinsic density (>7 g·cm^{-3}) implies that WO_3 has the higher volumetric power/energy performance.[19] It is also highly resistant to strong acids. Chang et al. previously reported that the utilization of crystalline tungsten oxide mixtures as electrodes resulted in a capacitance of up to 290 F·g^{-1};[20] Yoon et al. reported a specific capacitance of 451 F·cm^{-3} from a mesoporous nanostructured WO_3.[21] Jeong et al. fabricated WO_3 nanoparticle impregnated ZrO_2−SiO_2 sheets for energy storage and reported a capacitance of 313 F·g^{-1}.[22] It is well-known that 3D hierarchical nanostructures boast high surface/body ratios, large surface areas, and higher permeability, thus being beneficial to the enhancement of supercapacitor performance.[23,24] Hercule et al. reported that the hierarchical architecture allows for the synergistic contribution of mixed electrode materials and leads to a better electrochemical

Received: September 30, 2015
Accepted: November 30, 2015
Published: November 30, 2015

DOI: 10.1021/acsami.5b09257
ACS Appl. Mater. Interfaces 2015, 7, 27845−27852

performance.[25] In this work, all-solid-state flexible MSCs, as shown in Figure 1, were prepared by a scalable process of direct laser patterning on crack-free flexible WO_3/polyvinylidene fluoride (PVDF)/multiwalled carbon nanotubes (MWCNTs) films containing porous hierarchically structured tungsten trioxide (WO_3) nanomaterials (up to 50 wt %) and limited binder (PVDF, <25 wt %). The work leads to an areal capacitance of 62.4 mF·cm^{-2} and a volumetric capacitance of 10.4 F·cm^{-3}, exceeding that of graphene based flexible MSCs[3] by a factor of 26 and 3, respectively.

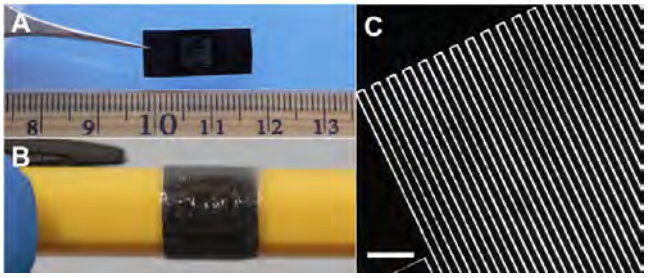

Figure 1. Images of MSCs. (A) A freestanding MSC, (B) wrapped onto a pen, (C) under an optical microscope (scale bar: 500 μm).

■ RESULTS AND DISCUSSION

Most of the nanomaterials based MSCs reported previously are too thin to provide sufficient energy.[1,19] The high energy and power densities reported from thin electrodes do not scale up with the thickness of the electrode, while thick electrodes are conducive to higher energy densities, but may decrease charge/discharge rates, thus lowering power.[26] We designed and fabricated interdigitated electrodes with minimized width of, and gap between, the fingers to allow for more active nanomaterials on the electrode areas, lower internal impedance, and higher charge/discharge rates (Figure 2). In addition, the fact that only part of the electrodes (<10 μm) near the geometric electrode/electrolyte interface can be utilized as a result of the poor penetration of solid-state electrolyte hampers the practicality for thick electrode active nanomaterials being used for solid-state SCs in traditional sandwiched structures.[27] Therefore, the interdigital structure is essential to the application of thick nanomaterials-containing electrodes in all-solid-state SCs by downsizing each finger electrode, thus shortening the distance for solid-state electrolytes to wet.

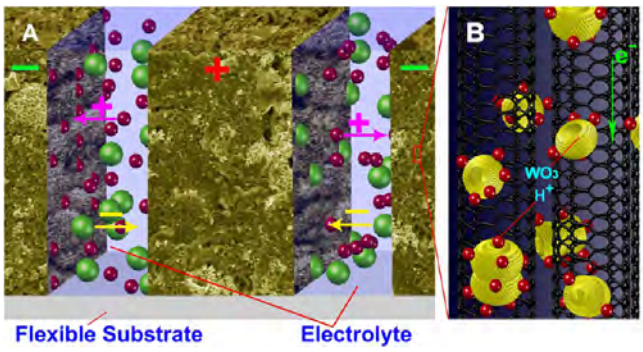

Figure 2. Schematics of the mechanism of MSCs. (A) MSC design with interdigitated electrodes in the form of narrow fingers and with minimized spacing in between. (B) Protons intercalate with pseudocapacitive materials.

Hierarchically Nanostructured Tungsten Oxide Fabrication. Different from the hydrothermal processes used for the fabrication of nanostructured tungsten oxide at 120−180 °C in autoclaves,[28,29] we developed an acid-directed hydrothermal process to form hierarchical tungsten oxide nanostructures at low temperature (70−90 °C) under atmospheric conditions by leveraging the chelating ability of citric acid. By changing the ratio of Na_2WO_4 and citric acid solutions, reactant concentrations, and pH value, a family of tungsten oxide nanostructures could be prepared as shown in Figures 3 and S1. With the decreasing concentrations of reactants and pH value, the morphology of tungsten oxide precipitates varied from spheres comprised of needle bundles, nanoplates, and nest-like hollow spheres to spheres consisting of nanoplates with increasing duration. In this work, the WO_3 powder with nest-like morphology (Figure 3D) was used as the pseudocapacitance material for the MSCs on account of its hierarchical morphology and relatively higher yield than the other two (Figure 3E,F) produced by our growth method. Figure 4 displays more details of the nanostructured materials. Figure 4A,B shows that our tungsten oxide nanostructures consisted of a few highly porous spherical shells self-assembled by nanoplates of 30−80 nm in thickness. XRD spectra (Figure 4F) reveals that only the spectrum of $WO_3{\cdot}H_2O$ could be observed with preferential growth in the (111) direction (ICDD PDF 00-043-0679). It was converted to WO_3 after annealing in air at 500 °C for 2 h to remove citrate ligands. Accordingly, the smooth surface of the nanoplates in the nest-like nanostructures became rough and even porous (Figure 4C,D). The high resolution transmission electron microscopy (HRTEM) image in Figure 4E shows lattice fringes of scraped hierarchical WO_3 nanostructures. The interplanar spacing values of 0.367, 0.379, and 0.264 nm correspond to the crystal planes (200), (020), and (220) of the monoclinic WO_3 phase (ICDD PDF 04-005-4272), respectively.

To prevent crack formation, the freestanding electrode films were prepared prior to integration onto supporting substrates (Surlyn, 25 μm), thereby avoiding the restraint from the substrate against their natural contraction during the drying process. MWCNTs were used to improve the electrical conductivity of the electrodes, and likewise, acetylene carbon black was used for comparison. PVDF possesses a high dielectric constant and excellent chemical corrosion resistance and is commonly used as a binder in energy storage systems.[30,31] The interconnected hollow structures of WO_3 powder in the composite not only offered spaces to accommodate the solid-state electrolyte and low hurdles for ionic diffusion but also functioned as a scaffold to maintain the porous structure of the electrodes. These benefits remained even after the electrode was compressed for better electric conductivity before usage, as shown in Figure 5A. Figure 5B,C shows that the thickness of compressed WO_3/PVDF/MWCNTs (0.5:0.25:0.25) film is ∼60 μm, and the outer surface of WO_3 structures was fully covered by PVDF/MWCNTs matrix. Figure S2A,B shows that the dry film was freestanding and crack-free even if its surface area shrunk down to ∼20% of the initial casting size. Figure S2C,D demonstrates the excellent flexibility of WO_3/PVDF/C films, both in the freestanding form and with the use of a Surlyn substrate.

Electrochemical Measurement of Electrodes. To investigate the impact of film compositions on its electro-

DOI: 10.1021/acsami.5b09257
ACS Appl. Mater. Interfaces 2015, 7, 27845−27852

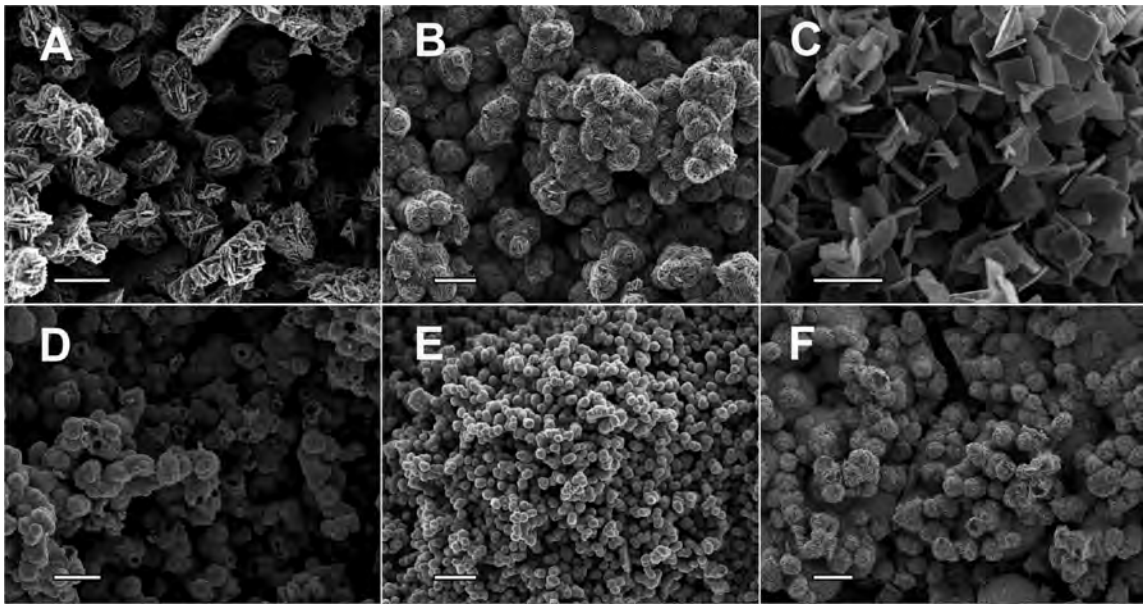

Figure 3. SEM images of hierarchical tungsten oxide nanostructure with different growth conditions. (A) pH = 1.5, Na_2WO_4 (0.25 M)/citric acid (0.25 M) = 1:1, 90 °C, 0.5 h; (B) pH = 1, Na_2WO_4 (0.25 M)/citric acid (0.25 M) = 1:1, 90 °C, 0.5 h; (C) pH = 1, Na_2WO_4 (0.125 M)/citric acid(0.125 M) = 1:1, 90 °C, 1 h; (D) pH = 0.5, Na_2WO_4 (0.08 M)/citric acid (0.10 M) = 0.8, 90 °C, 2 h; (E) pH = 0.5, Na_2WO_4 (0.05 M)/citric acid (0.10 M) = 1:2, 90 °C, 6 h; (F) pH = 0.5, Na_2WO_4 (0.02 M)/citric acid (0.10 M) = 1:2, 90 °C, 8 h. Scale bars are 5, 10, 1, 5, 10, and 10 μm in (A−F), respectively.

chemical properties, four types of WO_3/PVDF/C composite films (films 1 to 4) were fabricated and used as direct electrodes for electrochemical studies (Figure S3). Their cyclic voltammograms were characterized from −0.2 to 0.8 V and are summarized in Figure 6. The curves demonstrate an evolution from a rectangular shape for the PVDF/MWCNT electrode to a dolphin-like shape for electrodes with increasing WO_3 components, suggesting varying contributions of pseudocapcitance and electric double layer (EDL) behavior.[20,32]

Film electrodes with a high level of WO_3 (50%) exhibited higher capacitances, with a maximum specific capacitance of 77 $F\cdot cm^{-3}$ at a scan rate of 5 $mV\cdot s^{-1}$ for film 1. By replacing MWCNTs with the same mass of acetylene carbon black in film 2, the cyclic voltammetry (CV) curves (Figure 6C) demonstrate a relatively narrow tip within 0.6−0.8 V, indicating poorer EDL capacitance (EDLC) due to smaller specific surface area of acetylene carbon black than MWCNTs. However, the volumetric capacitance of film 2 was still higher than films 3 and 4 containing less WO_3. The shape in Figure 6D (film 3) exhibits a higher EDLC contribution than pseudocapacitance to the total capacitance, resulting from the higher ratio of MWCNTs to WO_3. By assuming that the capacitance of the four electrodes at high potential range (0.6−0.8 V) is pure EDLC and does not change over the whole voltage range, the respective contribution of EDLC and pseudocapacitance to the overall capacitance can be plotted (Figure S4) and evaluated.[33,34] The contribution of pseudocapacitance to the whole capacitance of the electrodes is 46%, 70%, and 44% for films 1, 2, and 3, respectively. The higher value for film 2 is due to the relatively low EDLC of acetylene carbon black compared with film 1.

Brunauer−Emmett−Teller (BET) surface area analysis and Barrett−Joyner−Halenda (BJH) pore size and volume analysis (Figure S5 and Table S1) show that the presence of hierarchically nanostructured WO_3 increases the pore size of electrode by 25% comparing the data of film 1 (50% WO_3) and film 4 (no WO_3). Film 2 showed the lowest pore size because of the smaller surface area of acetylene carbon black than MWCNTs. Although WO_3 reduced the total pore volume of electrodes (partially because of the low density of MWCNT materials), the contribution of pseudocapacitance significantly outweighs the negative impact of this materials.

Fabrication and Performance of MSCs. Among the processes used to fabricate MSCs, laser technology is especially promising as it allows for scalable fabrication of interdigital MSCs. Cao et al. fabricated an on-chip MSC using a laser to pattern MoS_2 nanosheets and reported an areal capacitance of 8 $mF\cdot cm^{-2}$.[5] Here, a femtosecond laser was used to fabricate the interdigital structure with high width-to-depth aspect ratio on WO_3/PVDF/MWCNTs composite films. The minimized thermal effects of the laser ablation kept the narrow finger electrodes from breaking. WO_3/PVDF/MWCNTs composite films were fixed onto a flat and rigid surface for the subsequent laser patterning as shown in Figure 7. The WO_3/PVDF/MWCNTs film functioned as both active material and electron collector for MSCs. Surlyn served as an adhesive and substrate to stabilize the finger electrodes during the laser patterning, while low tack polyethylene (PE) tape was used to facilitate the detachment of MSCs from the glass slides following drop casting of poly(vinyl alcohol) (PVA)/H_2SO_4 electrolyte and removal of excess water.

Film 1 was used to fabricate MSCs. The photo image of MSC is shown in Figures 1 and S6 with a finger width of 200 and 30 μm of spacing. After the laser ablation, the surface of finger electrodes was covered by a 2 μm layer of WO_3 nanoparticles with diameters of 100 nm as shown in Figure S7. XRD spectra (Figure S8) show that new phases in small amount were formed during the laser ablation and were associated with WO_2 (2θ = 36.84) and W (2θ = 40.16) due to the reduction reaction of carbon with tungsten trioxide.[35] Energy dispersive X-ray (EDX) linescan spectra (Figure S9) indicate that the interior composition was not changed within

DOI: 10.1021/acsami.5b09257
ACS Appl. Mater. Interfaces 2015, 7, 27845−27852

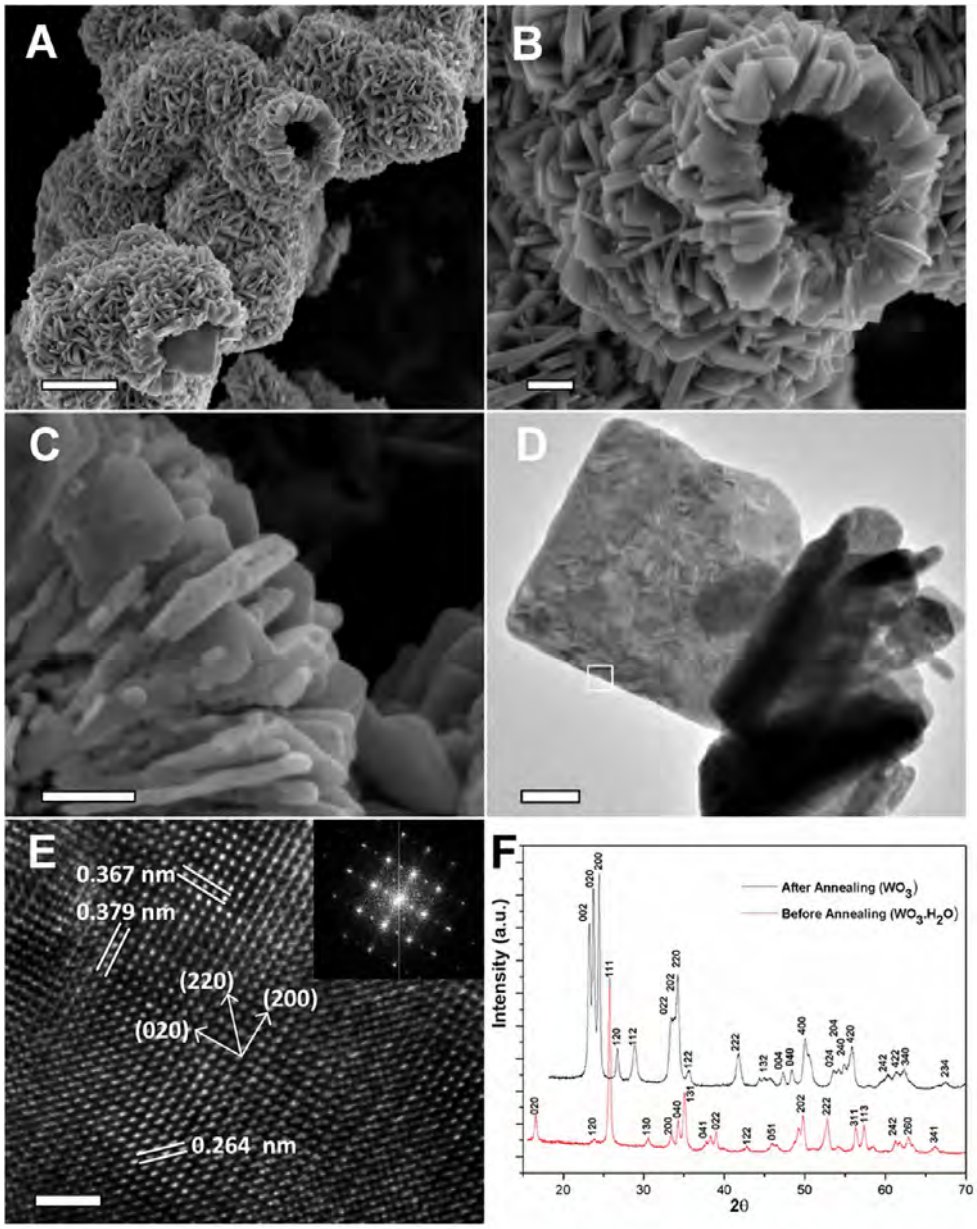

Figure 4. Characterization of nanostructured tungsten oxide. (A, B) SEM images of nest-like $WO_3 \cdot H_2O$ and (C) WO_3 (after annealing at 500 °C in air for 2 h). (D) TEM images of WO_3. (E) HRTEM images of WO_3 (inset, the fast-Fourier transform image). (F) XRD spectra of tungsten oxide before and after annealing. Scale bars are 1 μm, 200 nm, 200 nm, 100 nm, and 2 nm in (A−E), respectively.

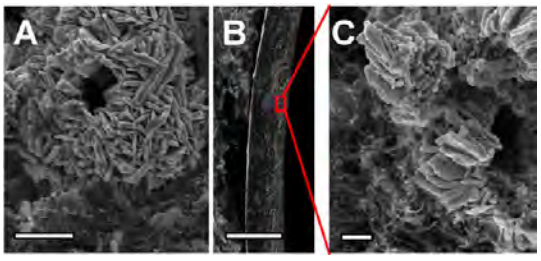

Figure 5. Scanning electron microscopy (SEM) images of a compressed WO_3/PVDF/MWCNTs (0.5:0.25:0.25) film. (A) Top perspective view; (B, C), cross-sectional views. Scale bars are 1, 100, and 500 μm in (A−C), respectively.

the finger electrode structure after the laser ablation. The laser ablation could burn the carbon and PVDF out and cause slightly higher composition of tungsten and oxygen only in the surface area of the finger electrodes. Figures 1A,B and S6A,B show photographs of a prepared flexible MSC before and after detachment from the glass substrate. In our experiments, Film 4 (PVDF/MWCNTs) was burned out during the laser ablation, failing to form interdigital structures. Hence, the metal oxide (WO_3) also presumably played a role as flame retardant in our work. Our use of pulsed laser also benefited the laser patterning, as it reduces the risk of burning of the polymer substrates towing to excessive ablation. MSCs were ready for electrochemical testing after being coated by PVA/H_2SO_4 hydrogel electrolyte and removal of excess water (>4 h). PVA/H_2SO_4 hydrogel played a critical role in keeping the fingers from contacting one another and breaking during the detachment from the substrate. Three types of MSCs were constructed with finger widths of 50, 100, and 200 μm,

DOI: 10.1021/acsami.5b09257
ACS Appl. Mater. Interfaces 2015, 7, 27845−27852

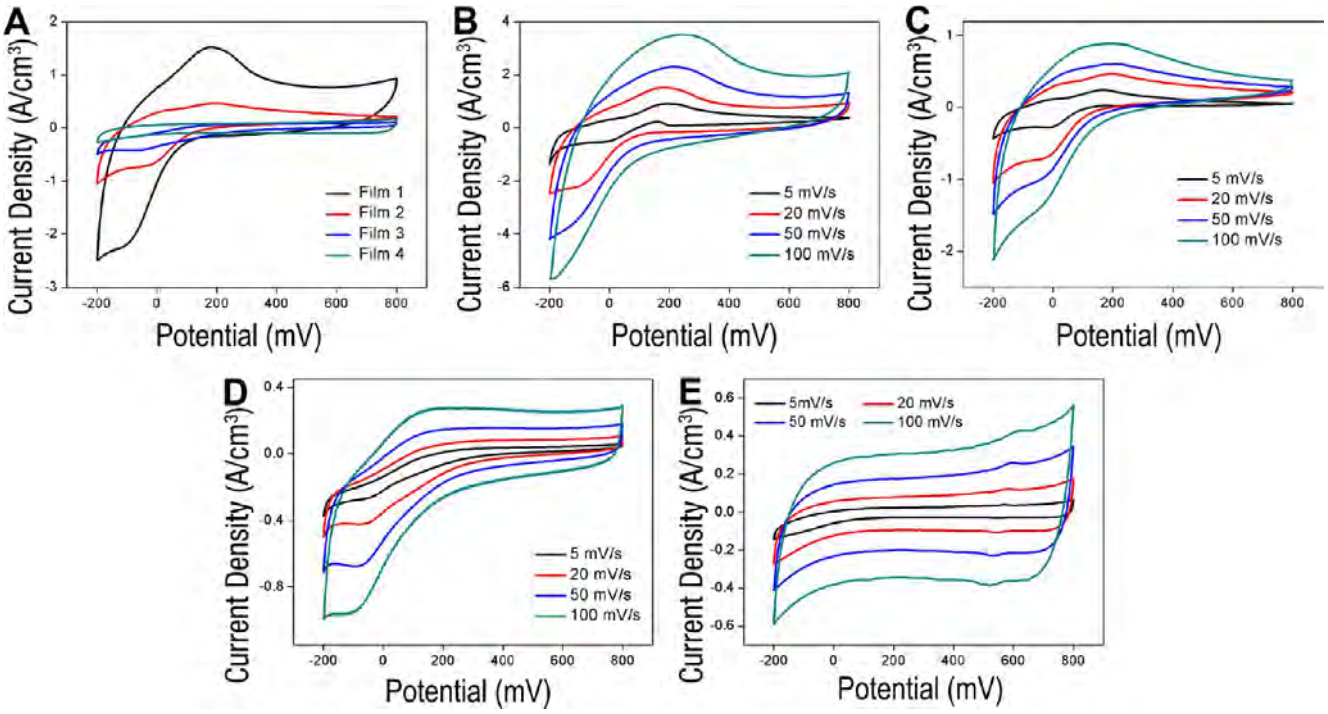

Figure 6. Electrochemical performance of WO_3/PVDF/C electrodes with an Ag/AgCl reference electrode. (A) CV profiles of film 1 (WO_3/PVDF/MWCNTs 0.5:0.25:0.25), film 2 (WO_3/PVDF/acetylene carbon black 0.5:0.25:0.25), film 3 (WO_3/PVDF/MWCNTs 0.2:0.55:0.25), and film 4 (PVDF/MWCNTs 0.75:0.25) in 2 M H_2SO_4 at a scan rate of 20 mV/s. (B−E) CV curves of film 1, 2, 3, and 4, respectively, at different scan rates in 2 M H_2SO_4 solution.

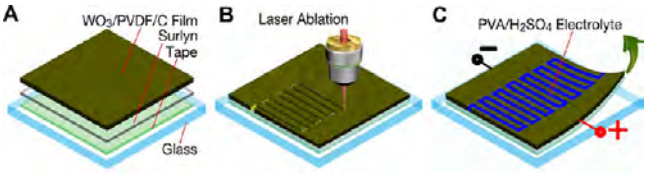

Figure 7. Schematic of the fabrication process for MSCs. (A) The WO_3/PVDF/MWCNTs films formed were attached onto rigid substrate. (B) Laser patterning. (C) Detachment of as prepared MSCs.

respectively. The spacing between neighboring fingers was ∼30 μm. Figures 8, S10, and S11 display the electrochemical performance of these MSCs. The shape of CV curves is affected by both the electron−proton transfer mechanism at the surface of pseudocapacitance materials and the internal resistance.[36] At the high scan rate of 100 mV·s^{-1}, the CVs in Figure 8A,B,E retain a nearly symmetrical rectangular shape and instantaneous response upon the reversal of applied voltage, indicating a high power of our MSCs.[37] The highest areal and volumetric capacitance achieved was 62.4 mF·cm^{-2} and 10.4 F·cm^{-3}, respectively, from the MSC with 100 μm finger electrodes, measured at a scan rate of 20 mV·s^{-1} and 0−0.8 V voltage window as shown in Figure 8C. A 17% decrease to 8.65 F·cm^{-3} was observed when the scan rate was increased to 100 mV·s^{-1}. The interdigital structure significantly improved ionic diffusion in thick electrodes, which explains the improvement in the specific capacitance of the MSC electrode up to 41.6 F·cm^{-3}, even higher than that of electrodes in a liquid electrolyte (2 M H_2SO_4) of a three-electrode system (36.8 F·cm^{-3}).

Although the MSC with 50 μm-wide fingers has a larger cross-sectional surface area than 100 μm-wide fingers and thus a higher expected volumetric capacitance, it has a lower relative capacitance (7.7 F·cm^{-3}); this can be attributed to a larger impact of the increasing electric resistance of the smaller finger electrode on its performance. The lowest capacitance (3.05 F·cm^{-3}) of the MSCs with 200 μm-wide fingers indicates that the interdigitated design has less contribution when the size of the fingers increases far beyond the wetting distance of the solid-state electrolyte. Wider fingers, though, have lower internal resistance, shown by the electrochemical impedance spectroscopy (EIS) (Figure 8D). The EIS was measured in the frequency range of 1−1000 Hz. Compared with 1.5−2.5 Ω of resistance shown in the EIS spectra for four types of film electrodes in 2 M H_2SO_4 solution in the form of the Nyquist plots (Figure S12), the microsized finger electrodes mainly resulted in the increased internal resistance. The double layer low frequency spikes all start at ∼9 Hz, and the steep lines indicate nonideal capacitive response due to the surface roughness and nonuniform active layer thickness. The steep slope of the double layer spike also makes the Warburg impedance less conspicuous.[38,39]

When the spacing between neighboring fingers increased from 30 to 50 μm (finger width = 100 μm), the MSC showed a volumetric specific capacitance of 6.29 F·cm^{-3} at a scan rate of 20 mV·s^{-1} as shown in Figure S13. The decreased performance could be associated with the reduction of active materials on electrodes, given the total device area. Figures 8E and S14 show that specific capacitance calculated from CV curves of an MSC after detachment from the glass substrate did not experience significant variation under different bending conditions. The cyclic properties of MSCs were also tested; a 20% decrease was observed after 1000 cycles on a glass slide and 2000 cycles detached. The typical galvanostatic charge/discharge curves of the MSC collected at different current densities are shown in Figure 8F. The highest energy density and power density was found to be 0.97 mWh·cm^{-3} and 62 W·cm^{-3}, respectively.

DOI: 10.1021/acsami.5b09257
ACS Appl. Mater. Interfaces 2015, 7, 27845−27852

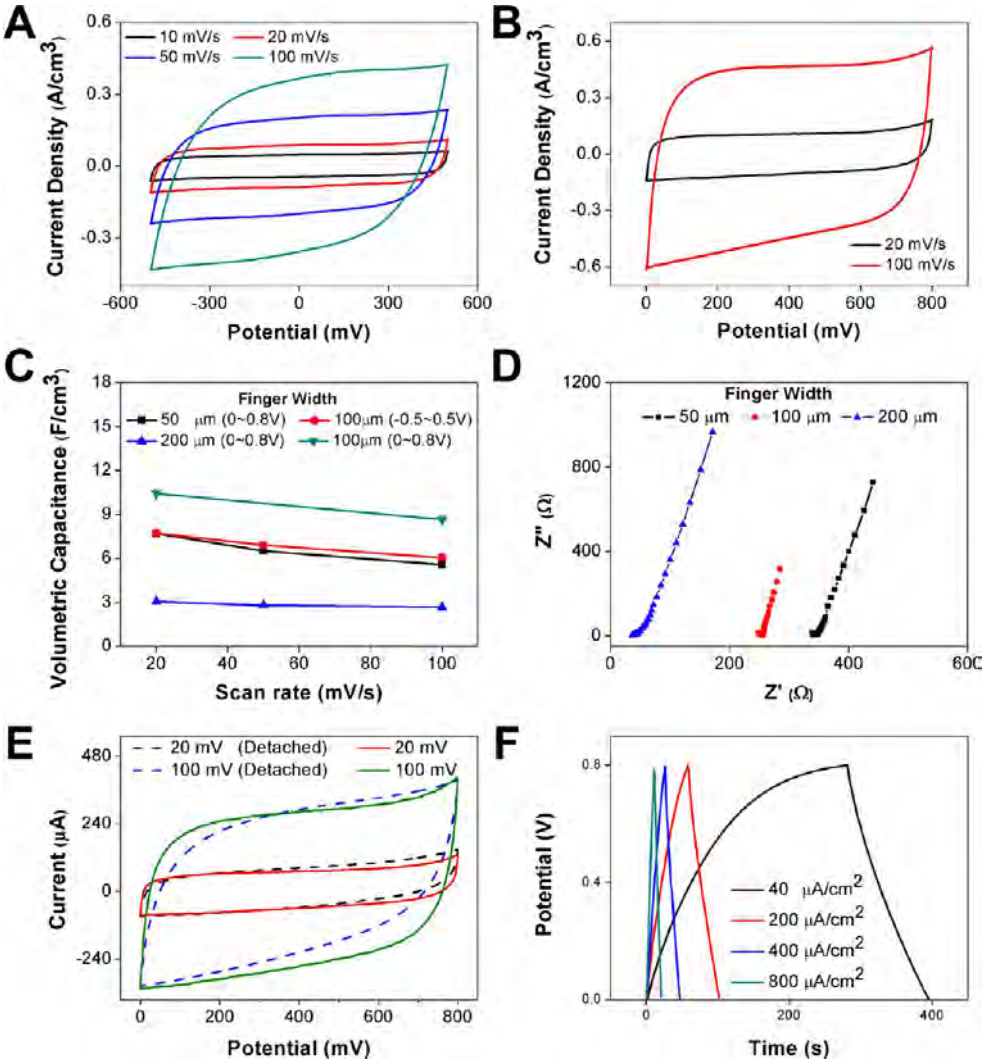

Figure 8. Electrochemical performance of MSCs. (A,B) CV curves of WO_3/PVDF/MWCNTs (0.5:0.25:0.25) based MSCs with the finger width of 100 μm at deferent potential windows and scan rates. (C) Volumetric capacitance and (D) EIS of MSCs with different finger widths. (E) CV curves of MSC before and after detachment from the glass substrate. (F) Galvanostatic charge/discharge curves of MSCs (finger width of 200 μm) collected at different current densities.

■ CONCLUSION

This work demonstrated an advantageous method to fabricated all-solid-state flexible MSCs based on self-standing, crack-free nanomaterials containing composite films. Nest-like WO_3 nanostructures prepared with a low temperature hydrothermal process were used as pseudocapacitive materials for MSCs. The increasing composition of WO_3 in the composite electrodes contributed to higher specific capacitances. The interdigital structure realized by direct laser patterning on thick composite electrode was the key to the ultrahigh volumetric capacitance and energy density of our flexible MSCs. The MSC with fingers with a width of 100 μm and a spacing of 30 μm exhibited the highest energy storage performance. The performance of these MSCs can be further enhanced by optimizing electrode materials, the wetting property between the electrode and the electrolyte, and the laser processing.

■ EXPERIMENTAL SECTION

Synthesis of Porous Hierarchical WO_3 Nanostructures and Characterization. In a typical experiment, 100 mL of Na_2WO_4 (0.08 M) solution and 100 mL of citric acid (0.10 M) were added into a glass container, followed by adding HCl (5 M) to the container to adjust the pH value to 0.5, monitored by pH tester (Oakton, EW-35634-30). The container covered by a glass slide was subsequently placed in a furnace maintained at 90 °C for 2 h. The final reactive solution was clear, and the yellow nest-like $WO_3{\cdot}H_2O$ precipitates could be found on the bottom and side wall of the reactor. These precipitates were washed with DI water and centrifuged three times to remove impurities. The $WO_3{\cdot}H_2O$ powder was dried in air at 100 °C and then annealed in air at 500 °C for 2 h. All chemicals were bought from Sigma-Aldrich. The prepared tungsten oxide nanomaterials were characterized by scanning electron microscopy (LEO 1530 FESEM), transmission electron microscopy (Tecnai TF-30), and XRD spectroscopy (Bruker D8 discovery, operating with a Cu Kα radiation source filtered with a graphite monochromator [λ = 1.5406 Å]).

Femtosecond Laser Process. We used a vertical-polarized laser (Uranus2000-1030-1000, PolarOnyx) with pulse duration of 700 fs, a wavelength of 1030 nm, and a repetition rate of 120 kHz to form the comb structures on WO_3/PVDF/MWCNTs films directly. The diameter of the focal spot was 1.5 μm. A mechanical shutter was used to turn the laser on and off. A neutral density attenuator and polarizer were used to control the power and polarization of the laser beam. The sample was mounted on a computer-controlled *xyz* stage (Newport XMS-160, XMS-100, and GTS-30 V for the *x*-axis, *y*-axis, and *z*-axis, respectively). By translating the sample, the microstructures

DOI: 10.1021/acsami.5b09257
ACS Appl. Mater. Interfaces 2015, 7, 27845−27852

were patterned by the focused laser pulses, and a CCD camera and relay lens were used for real-time monitoring of the patterning process. The laser energy was 2.45 μJ per pulse, and the scanning speed was 0.5 mm·s^{-1}.

Fabrication for MSCs and Electrochemical Characterizations. The compressed WO_3/PVDF/MWCNT film (~60 μm) was first attached onto a layer of Surlyn (25 μm, Solaronix) by heating at 110 °C for 20 min. Then, the flexible composite was adhered through the same heating process to the surface of a low tack PE tape (75 μm) which had been preliminarily covered on a glass slide as shown in Figure 7A. The thickness of electrodes used was determined by the power of our laser system. The WO_3/PVDF/C electrode with substrates was then patterned by the laser to form interdigital structures (Figure S15). The WO_3/PVDF/C films functioned as both active materials for energy storage and electron collectors. PVA/H_2SO_4 hydrogel, as an electrolyte, was prepared by mixing 6 g of PVA (M_w = 89,000−98,000, Sigma-Aldrich) powder, 6 g of H_2SO_4 (Sigma-Aldrich), and DI water (60 mL). The mixture was heated at 85 °C under stirring until the solution turned clear. WO_3/PVDF/C electrodes and MSCs were characterized by CV and electrochemical impedance spectroscopy using a BAS 100B Electrochemical Analyzer. Galvanostatic charge/discharge measurements were conducted using a Keithley 2400 source meter and an Agilent 34411A 61/2 digital multimeter. The CV of electrodes was measured in a three-electrode system (vs an Ag/AgCl reference electrode). A platinum foil was placed 1 cm away from WO_3/PVDF/C electrodes as the counter electrode.

■ ASSOCIATED CONTENT

Ⓢ Supporting Information

The Supporting Information is available free of charge on the ACS Publications website at DOI: 10.1021/acsami.5b09257.

Methods for the preparation of electrode films and pastes, as well as calculations. Photo and SEM images of WO_3PVDF/MWCNTs (0.5:0.25:0.25) films. More photo images and electrochemical measurements of MSCs. Design and dimensions of the MSCs. (PDF)

■ AUTHOR INFORMATION

Corresponding Author

*E-mail: hongrui@engr.wisc.edu.

Author Contributions

¶X. Huang and H. Liu contributed to the work equally.

Notes

The authors declare no competing financial interest.

■ ACKNOWLEDGMENTS

This work was supported by the National Institutes of Health (Grant No. 1DP2OD008678-01). The authors thank B. Gundlach for technical assistance and proofreading the manuscript and Dr. G. Lin for discussions and assistance.

■ REFERENCES

(1) Chmiola, J.; Largeot, C.; Taberna, P. L.; Simon, P.; Gogotsi, Y. Monolithic Carbide-Derived Carbon Films for Micro-Supercapacitors. *Science* **2010**, *328*, 480−483.

(2) Winter, M.; Brodd, R. J. What Are Batteries, Fuel Cells, and Supercapacitors? *Chem. Rev.* **2004**, *104*, 4245−4269.

(3) El-Kady, M. F.; Kaner, R. B. Scalable Fabrication of High-Power Graphene Micro-Supercapacitors for Flexible and On-Chip Energy Storage. *Nat. Commun.* **2013**, *4*, 1475−1483.

(4) Shen, C.; Wang, X.; Zhang, W.; Kang, F. A High-Performance Three-Dimensional Micro-Supercapacitor Based on Self-Supporting Composite Materials. *J. Power Sources* **2011**, *196*, 10465−10471.

(5) Cao, L.; Yang, S.; Gao, W.; Liu, Z.; Gong, Y.; Ma, L.; Shi, G.; Lei, S.; Zhang, Y.; Zhang, S.; Vajtai, R.; Ajayan, P. M. Direct Laser-Patterned Micro-Supercapacitors from Paintable MoS_2 Films. *Small* **2013**, *9*, 2905−2910.

(6) Beidaghi, M.; Gogotsi, Y. Capacitive Energy Storage in Micro-Scale Devices: Recent Advances in Design and Fabrication of Micro-Supercapacitors. *Energy Environ. Sci.* **2014**, *7*, 867−884.

(7) Gao, W.; Singh, N.; Song, L.; Liu, Z.; Reddy, A. L. M.; Ci, L.; Vajtai, R.; Zhang, Q.; Wei, B.; Ajayan, P. M. Direct Laser Writing of Micro-Supercapacitors on Hydrated Graphite Oxide Films. *Nat. Nanotechnol.* **2011**, *6*, 496−500.

(8) Xiao, X.; Ding, T.; Yuan, L.; Shen, Y.; Zhong, Q.; Zhang, X.; Cao, Y.; Hu, B.; Zhai, T.; Gong, L.; Chen, J.; Tong, Y.; Zhou, J.; Wang, Z. L. WO_{3-x}/MoO_{3-x} Core/Shell Nanowires on Carbon Fabric as an Anode for All-Solid-State Asymmetric Supercapacitors. *Adv. Energy Mater.* **2012**, *2*, 1328−1332.

(9) Meng, C.; Liu, C.; Chen, L.; Hu, C.; Fan, S. Highly Flexible and All-Solid-State Paperlike Polymer Supercapacitors. *Nano Lett.* **2010**, *10*, 4025−4031.

(10) Wang, K.; Zou, W.; Quan, B.; Yu, A.; Wu, H.; Jiang, P.; Wei, Z. An All-Solid-State Flexible Micro-Supercapacitor on a Chip. *Adv. Energy Mater.* **2011**, *1*, 1068−1072.

(11) Hu, C.; Song, L.; Zhang, Z.; Chen, N.; Feng, Z.; Qu, L. Tailored Graphene Systems for Unconventional Applications in Energy Conversion and Storage Devices. *Energy Environ. Sci.* **2015**, *8*, 31−54.

(12) Wang, D.; Li, F.; Zhao, J.; Ren, W.; Chen, Z.; Tan, J.; Wu, Z.; Gentle, I.; Lu, G.; Cheng, H. Fabrication of Graphene/Polyaniline Composite Paper via in Situ Anodic Electropolymerization for High-Performance Flexible Electrode. *ACS Nano* **2009**, *3*, 1745−1752.

(13) Augustyn, V.; Come, J.; Lowe, M. A.; Kim, J. W.; Taberna, P. L.; Tolbert, S. H.; Abruña, H. D.; Simon, P.; Dunn, B. High-Rate Electrochemical Energy Storage Through Li^+ Intercalation Pseudocapacitance. *Nat. Mater.* **2013**, *12*, 518−522.

(14) Lee, G.; Kim, D.; Yun, J.; Ko, Y.; Cho, J.; Ha, J. S. High-Performance All-Solid-State Flexible Micro-Supercapacitor Arrays with Layer-by-Layer Assembled MWNT/MnO_x Nanocomposite Electrodes. *Nanoscale* **2014**, *6*, 9655−9664.

(15) Chen, Z.; Augustyn, V.; Wen, J.; Zhang, Y.; Shen, M.; Dunn, B.; Lu, Y. High-Performance Supercapacitors Based on Intertwined CNT/V_2O_5 Nanowire Nanocomposites. *Adv. Mater.* **2011**, *23*, 791−795.

(16) Jing, G.; Ma, J. Formation of Circular Crack Pattern in Deposition Self-Assembled by Drying Nanoparticle Suspension. *J. Phys. Chem. B* **2012**, *116*, 6225−6231.

(17) Bohnke, O.; Robert, G. Electrochemical Lithium Incorporation into WO_3 and MoO_3 Thin Films. *Solid State Ionics* **1982**, *6*, 115−120.

(18) Wen, R. T.; Granqvist, C. G.; Niklasson, G. A. Eliminating Degradation and Uncovering Ion-Trapping Dynamics in Electrochromic WO_3 Thin Films. *Nat. Mater.* **2015**, *14*, 996−1001.

(19) Jo, C.; Hwang, J.; Song, H.; Dao, A. H.; Kim, Y. T.; Lee, S. H.; Hong, S. W.; Yoon, S.; Lee, J. Block-Copolymer-Assisted One-Pot Synthesis of Ordered Mesoporous WO_{3-x}/Carbon Nanocomposites as High-Rate-Performance Electrodes for Pseudocapacitors. *Adv. Funct. Mater.* **2013**, *23*, 3747−3754.

(20) Chang, K. H.; Hu, C.; Huang, C.; Liu, Y.; Chang, C. Microwave-Assisted Hydrothermal Synthesis of Crystalline WO_3·WO_3·0.5H_2O Mixtures for Pseudocapacitors of the Asymmetric Type. *J. Power Sources* **2011**, *196*, 2387−2392.

(21) Yoon, S.; Kang, E.; Kim, J. K.; Lee, C. W.; Lee, J. Development of High-Performance Supercapacitor Electrodes Using Novel Ordered Mesoporous Tungsten Oxide Materials with High Electrical Conductivity. *Chem. Commun.* **2011**, *47*, 1021−1023.

(22) Jeong, G. H.; Lee, H. M.; Kang, J. G.; Lee, H.; Kim, C. K.; Lee, J. H.; Kim, J. H.; Kim, S. W. ZrO_2−SiO_2 Nanosheets with Ultrasmall WO_3 Nanoparticles and Their Enhanced Pseudocapacitance and Stability. *ACS Appl. Mater. Interfaces* **2014**, *6*, 20171−20178.

(23) Mai, L.; Yang, F.; Zhao, Y.; Xu, X.; Xu, L.; Luo, Y. Hierarchical $MnMoO_4/CoMoO_4$ Heterostructured Nanowires with Enhanced Supercapacitor Performance. *Nat. Commun.* **2011**, *2*, 1−5.

DOI: 10.1021/acsami.5b09257
ACS Appl. Mater. Interfaces 2015, 7, 27845−27852

(24) Jiang, H.; Ma, J.; Li, C. Mesoporous Carbon Incorporated Metal Oxide Nanomaterials as Supercapacitor Electrodes. *Adv. Mater.* **2012**, *24*, 4197−4202.
(25) Hercule, K. M.; Wei, Q.; Khan, A. M.; Zhao, Y.; Tian, X.; Mai, L. Synergistic Effect of Hierarchical Nanostructured $MoO_2/Co(OH)_2$ with Largely Enhanced Pseudocapacitor Cyclability. *Nano Lett.* **2013**, *13*, 5685−5691.
(26) Kötz, R.; Carlen, M. Principles and Applications of Electrochemical Capacitors. *Electrochim. Acta* **2000**, *45*, 2483−2498.
(27) Kaempgen, M.; Chan, C. K.; Ma, J.; Cui, Y.; Gruner, G. Printable Thin Film Supercapacitors Using Single-Walled Carbon Nanotubes. *Nano Lett.* **2009**, *9*, 1872−1876.
(28) Zhao, Z. G.; Miyauchi, M. Shape Modulation of Tungstic Acid and Tungsten Oxide Hollow Structures. *J. Phys. Chem. C* **2009**, *113*, 6539−6546.
(29) Tian, Y.; Cong, S.; Su, W.; Chen, H.; Li, Q.; Geng, F.; Zhao, Z. Synergy of $W_{18}O_{49}$ and Polyaniline for Smart Supercapacitor Electrode Integrated with Energy Level Indicating Functionality. *Nano Lett.* **2014**, *14*, 2150−2156.
(30) Zhang, X.; Huang, X.; Li, C.; Jiang, H. Dye-Sensitized Solar Cell with Energy Storage Function through PVDF/ZnO Nanocomposite Counter Electrode. *Adv. Mater.* **2013**, *25*, 4093−4096.
(31) Huang, X.; Zhang, X.; Jiang, H. Energy Storage via Polyvinylidene Fluoride Dielectric on the Counterelectrode of Dye-sensitized Solar Cells. *J. Power Sources* **2014**, *248*, 434−438.
(32) Chen, J.; Li, W.; Wang, D.; Yang, S.; Wen, J.; Ren, Z. Electrochemical Characterization of Carbon Nanotubes as Electrode in Electrochemical Double-Layer Capacitors. *Carbon* **2002**, *40*, 1193−1197.
(33) Hu, Y.; Liu, H.; Ke, Q.; Wang, J. Effects of Nitrogen Doping on Supercapacitor Performance of a Mesoporous Carbon Electrode Produced by a Hydrothermal Soft-Templating Process. *J. Mater. Chem. A* **2014**, *2*, 11753−11758.
(34) Lin, Z.; Liu, Y.; Yao, Y.; Hildreth, O. J.; Li, Z.; Moon, K.; Wong, C.-p. Superior Capacitance of Functionalized Graphene. *J. Phys. Chem. C* **2011**, *115*, 7120−7125.
(35) Liang, C.; Tian, F.; Wei, Z.; Xin, Q.; Li, C. The Synthesis of Nanostructured W_2C on Ultrahigh Surface Area Carbon Materials via Carbothermal Hydrogen Reduction. *Nanotechnology* **2003**, *14*, 955−958.
(36) Jeong, Y. U.; Manthiram, A. Nanocrystalline Manganese Oxides for Electrochemical Capacitors with Neutral Electrolytes. *J. Electrochem. Soc.* **2002**, *149*, A1419−A1422.
(37) Si, W.; Yan, C.; Chen, Y.; Oswald, S.; Han, L.; Schmidt, O. G. On Chip, All Solid-State and Flexible Micro-Supercapacitors with High Performance Based on MnOx/Au Multilayers. *Energy Environ. Sci.* **2013**, *6*, 3218−3223.
(38) Prabaharan, S. R. S.; Vimala, R.; Zainal, Z. Nanostructured Mesoporous Carbon as Electrodes for Supercapacitors. *J. Power Sources* **2006**, *161*, 730−736.
(39) Ghaemi, M.; Ataherian, F.; Zolfaghari, A.; Jafari, S. M. Charge Storage Mechanism of Sonochemically Prepared MnO_2 as Supercapacitor Electrode: Effects of Physisorbed Water and Proton Conduction. *Electrochim. Acta* **2008**, *53*, 4607−4614.

DOI: 10.1021/acsami.5b09257
ACS Appl. Mater. Interfaces 2015, 7, 27845−27852